Patient Safety Starts Here

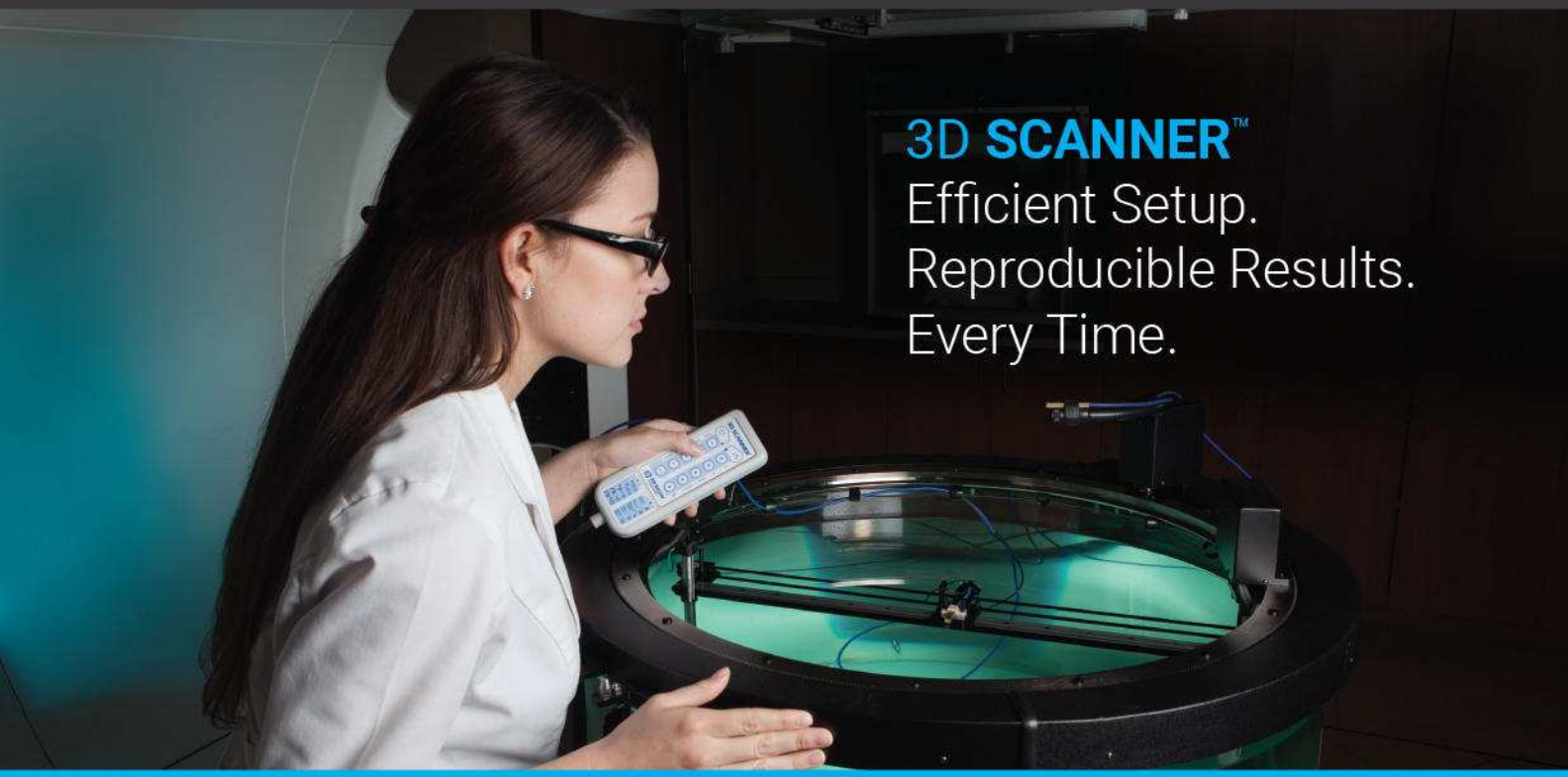

Want a credit for your existing tank? Click here.

"If you were to purchase a 3D Scanning System today, which would you choose?"

When asked this question by a 2016 MEDPHYS Mailing List survey, the majority of respondents chose the 3D SCANNER™ from Sun Nuclear. More than 550 facilities worldwide agree—the 3D SCANNER is their preferred water tank for accurate and efficient commissioning.

Visit sunnuclear.com to learn about these advantages and more.

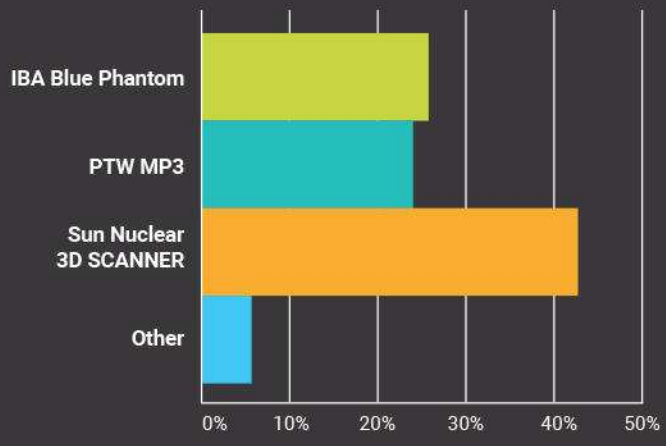

SUN NUCLEAR corporation

Using dual-energy x-ray imaging to enhance automated lung tumor tracking during real-time adaptive radiotherapy

Martin J. Menten,[a] Martin F. Fast, Simeon Nill, and Uwe Oelfke[b]
Joint Department of Physics at The Institute of Cancer Research and The Royal Marsden NHS Foundation Trust, London SM2 5NG, United Kingdom

(Received 23 February 2015; revised 20 October 2015; accepted for publication 28 October 2015; published 13 November 2015)

Purpose: Real-time, markerless localization of lung tumors with kV imaging is often inhibited by ribs obscuring the tumor and poor soft-tissue contrast. This study investigates the use of dual-energy imaging, which can generate radiographs with reduced bone visibility, to enhance automated lung tumor tracking for real-time adaptive radiotherapy.
Methods: kV images of an anthropomorphic breathing chest phantom were experimentally acquired and radiographs of actual lung cancer patients were Monte-Carlo-simulated at three imaging settings: *low-energy* (70 kVp, 1.5 mAs), *high-energy* (140 kVp, 2.5 mAs, 1 mm additional tin filtration), and *clinical* (120 kVp, 0.25 mAs). *Regular dual-energy* images were calculated by weighted logarithmic subtraction of high- and low-energy images and *filter-free dual-energy* images were generated from clinical and low-energy radiographs. The weighting factor to calculate the dual-energy images was determined by means of a novel objective score. The usefulness of dual-energy imaging for real-time tracking with an automated template matching algorithm was investigated.
Results: Regular dual-energy imaging was able to increase tracking accuracy in left–right images of the anthropomorphic phantom as well as in 7 out of 24 investigated patient cases. Tracking accuracy remained comparable in three cases and decreased in five cases. Filter-free dual-energy imaging was only able to increase accuracy in 2 out of 24 cases. In four cases no change in accuracy was observed and tracking accuracy worsened in nine cases. In 9 out of 24 cases, it was not possible to define a tracking template due to poor soft-tissue contrast regardless of input images. The mean localization errors using clinical, regular dual-energy, and filter-free dual-energy radiographs were 3.85, 3.32, and 5.24 mm, respectively. Tracking success was dependent on tumor position, tumor size, imaging beam angle, and patient size.
Conclusions: This study has highlighted the influence of patient anatomy on the success rate of real-time markerless tumor tracking using dual-energy imaging. Additionally, the importance of the spectral separation of the imaging beams used to generate the dual-energy images has been shown.
 [http://dx.doi.org/10.1118/1.4935431]

Key words: real-time adaptive radiotherapy, tumor tracking, lung tumor localization, dual-energy imaging, kV imaging

1. INTRODUCTION

Radiotherapy aims at depositing a lethal dose of ionizing radiation in tumors while minimizing radiation damage to surrounding healthy tissue, especially critical organs. Accurate dose delivery may be compromised by changes in the patient anatomy between the acquisition of the planning CT scan and the treatment or in between treatment fractions (interfractional motion) or during the irradiation itself (intrafractional motion). This effect is especially pronounced in the treatment of lung tumors as respiratory motion has been reported to cause tumor movement of up to a few centimeters.[1]

Real-time adaptive radiotherapy aims at modifying the dose delivery to dynamically account for the tumor motion. This may be achieved by moving the entire linear accelerator[2] or treatment head,[3] repositioning the patient with a robotic treatment couch[4,5] or by changing the treatment beam's aperture and position by moving the leaves of the multileaf collimator.[6–8] All aforementioned adaptation methods require information about the tumor position. One method of localizing the tumor is the surgical insertion of radioopaque markers near the tumor and their detection on kV or MV images.[9,10] Another method relies on the localization of several small resonant circuits by an electromagnetic array.[11,12] Either method is challenged by tumor deformation. Furthermore, surgical implantation of markers poses an additional burden for the patient and is not always possible due to comorbidities. Marker migration and cases of pneumonia have been reported as well.[3] On-board kV imaging devices feature on most modern linear accelerators and can be deployed to acquire radiographs frequently and quickly while the patient is undergoing treatment. In theory this allows markerless detection of the tumor position and deformation at the cost of an increased radiation dose to the patient. In reality automated localization of lung tumors in chest radiographs is often inhibited by ribs or soft-tissue anatomy obscuring the tumor and poor

soft-tissue contrast. Template matching algorithms (TMA) or other automated localization methods may inadvertently track prominent bone structures instead of the tumor.

Dual-energy (DE) imaging is able to generate radiographs with reduced bone visibility by exploiting the dependence of material contrast on the imaging energy.[13–15] Although this technology has been researched for clinical diagnostics for about 30 years, investigation of its use for real-time adaptive radiotherapy has only started recently with the wide-spread availability of digital flat-panel detectors (FPD) and the advent of fast kVp-switching x-ray tubes allowing acquisition of DE images at frequencies of up to 30 Hz.[16–19]

This work investigates the feasibility of using DE imaging to enhance automated localization of lung tumors for real-time adaptive radiotherapy. A modified Elekta x-ray volume imaging (XVI) system (Elekta AB, Stockholm, Sweden) was used to experimentally acquire DE images of an anthropomorphic breathing chest phantom. Additionally, a Monte Carlo (MC) simulation of the XVI system was created allowing generation of DE radiographs of actual lung cancer patients. It focusses on patient cases, in which the target might potentially be difficult to track on projection images due to small tumor volume, overlap of the tumor with other soft-tissue structures or large patient size. The usefulness of DE imaging for real-time tracking was evaluated with an automated TMA.

2. MATERIALS AND METHODS

2.A. Experimental acquisition of radiographs of an anthropomorphic breathing chest phantom

The Lucy anthropomorphic breathing chest phantom used in the experiments was developed for Paul-Scherrer-Institut (Villingen, Switzerland) by CSEM (Neuchâtel, Switzerland). It emulates a human torso including the lungs, skeleton, skin, heart, and a lung tumor (see Fig. 1). The air-tight lung compartment consists of a rubber balloon, which is filled with foam material as lung tissue. It is surrounded by the rib cage. When being inflated by a clinical respirator (bellavista 1000, imtmedical AG, Buchs, Switzerland), the lung compartment expands and a spherical tumor of 5 cm diameter inside, which is attached to the diaphragm, moves differentially to the rib motion. Once the inhalation phase is completed, foam pressing against the diaphragm from the outside deflates the lung compartment and returns the phantom to its original state.

The phantom was imaged with a modified Elekta XVI system featuring an XRD 1642 AP3 (PerkinElmer, Waltham, MA, USA) FPD. The system allows acquisition of radiographs with a resolution of 512×512 pixels and a pixel size of 0.8×0.8 mm^2 at detector level at a frequency of 30 Hz. Images were acquired at three different imaging settings. *Clinical* images were acquired at a tube voltage of 120 kVp (0.25 mAs) as has been suggested for the acquisition of chest radiographs.[20] *Low-energy* (LE) radiographs were acquired at 70 kVp (1.5 mAs). It was decided not to decrease the tube voltage further in order to maintain a low skin dose. *High-energy* (HE) images were acquired at 140 kVp (2.5 mAs). A 1.06 mm tin filter was inserted into the collimator cassette during acquisition of the HE images in order to increase the spectral separation between the HE and LE imaging spectra (see Sec. 2.C). Tin as filter material was selected for its sufficient attenuation, lack of spectrally distorting K-edges and nontoxicity.[21] All acquired images were gain-, offset-, and dead-pixel-corrected at each energy individually. The standard, empty F0 filter cassette without a bow-tie filter and the S20 collimator were used in the experiments.

The Lucy phantom was periodically inflated with a period length of 3 s, so that the lung tumor moved by 11 mm in superior–inferior (SI) and 9 mm in anterior–posterior (AP) direction. Dynamic imaging series of a breathing cycle were acquired at the three aforementioned imaging settings in AP as

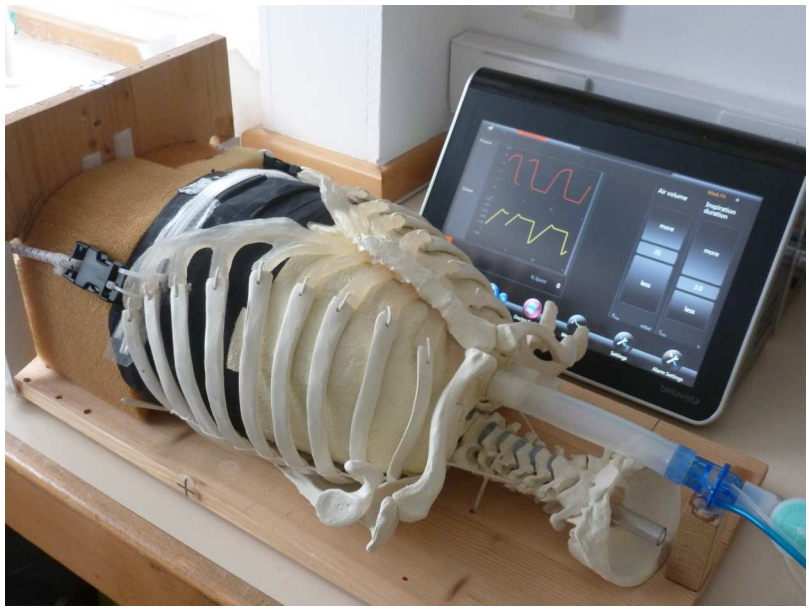

FIG. 1. Photograph of the Lucy phantom used in the experiments. The soft-tissue layer, which surrounds the ribs, is not attached to the phantom in the photograph.

well as left–right (LR) direction at a frequency of 30 Hz. As fast kVp-switching of the x-ray tube was not yet supported by the manufacturer, radiographs at alternating imaging settings could not be acquired in quick succession. Instead, each complete series was acquired sequentially and afterward manually aligned with each other according to the tumor position. Minor alignment errors of sub-pixel magnitude might remain due to the finite imaging frequency.

2.B. Generation of radiographs of lung cancer patients using Monte Carlo simulation

A MC simulation of the Elekta XVI system was developed using GEANT4, version 10.0, patch 1.[22] Simulation of the physical processes was based on the GEANT4 implementation of the PENELOPE models.[23] In order to speed up the simulation of the x-ray tube, uniform bremsstrahlung splitting with a splitting factor of 30 was implemented using the built-in runtime commands provided by GEANT4.

The MC simulation was split into two separate programs. The first program simulates the initial electron beam and the generation of the photon imaging beam. The active side of the anode, consisting of 95% tungsten and 5% rhenium, is tilted by 14° and the focal spot, 100 cm away from the isocenter, has a nominal focal spot size of 0.8×0.4 mm^2. Other components of the x-ray tube included in the simulation are the primary filter consisting of a 3.5 mm aluminum and a 0.1 mm copper layer and several supporting structures made out of thin polyethylene terephthalate glycol copolyester. The entire tube head is tilted by an additional 3.5°. These specifications were taken from the official Elekta XVI manual.[24] The LE, HE, and clinical imaging spectra used in the experimental setup were simulated with 2×10^{10} primary electrons each. During generation of the HE imaging spectrum, a 1.0 mm thick additional tin filter was simulated in the beam line. The position, energy, and momentum direction of each photon were stored into a phase space file as they pass the outer housing of the x-ray tube at 31.5 cm distance from the focal spot.

The second program simulates the previously generated imaging beam passing through the patient geometry, the treatment table, and the beam's interaction with the FPD. The voxelized patient geometry is created by transforming CT data into densities and material compositions using an algorithm adapted from Schneider *et al.*[25] Information about the composition of the iBEAM evo (Medical Intelligence Medizintechnik GmbH, Schwabmünchen, Germany) treatment table was obtained via personal communications with the manufacturer and from Smith *et al.*[26] Information regarding the geometry of the XRD 1642 AP3 FPD was obtained via personal communications with the manufacturer and the literature.[27–29] The source-to-detector distance measures 153.6 cm. For performance reasons, the simulation does not model the creation and transportation of optical photons in the scintillation layer and their detection in the amorphous silicon layer. Instead, the absorbed energy in the FPD's scintillation layer is determined. This 0.7 mm cesium iodide layer has a density of 3.85 g/cm^3 and is located behind a front plate consisting of 0.75 mm of aluminum and an additional layer of 0.5 mm graphite. The developed MC simulation was validated by comparing some common imaging quantities to a series of experimentally obtained results and values reported in the literature[30–32] (see Appendix A of the supplementary material[33] for a detailed description of the conducted validation simulations and experiments).

In order to generate patient radiographs, 4DCT data from stereotactic radiosurgery patients treated at our institution for lung cancer were used (written consent obtained). The CT scans were acquired with a Brilliance CT Big Bore (Philips Medical Systems, Cleveland, OH, USA) scanner. Six patients, who exhibited the largest tumor motion, were selected from a cohort of 19 (see Table I). Some of the chosen patient anatomies have features, which might potentially make tumor localization more difficult. Patient 2 has a very small tumor, which is attached to the posterior end of the diaphragm, the tumor of patient 3 deforms in SI direction and patient 4 is very large. In patient 6, a relatively small tumor is located near the aorta and upper branches of the bronchial tree. For each patient, chest radiographs of the peak-exhale as well as peak-inhale phase were simulated at the three aforementioned imaging settings, each at four imaging angles: 0° (AP), 45°, 90° (LR), and 135° (coordinate system according to IEC-61217). The ratio of primary photons was normalized to reflect the exposure settings of the experimental setup. Consequently, 9.45×10^9 photons were used to create a LE radiograph, while 7.50×10^9 and 7.88×10^9 photons were simulated to generate a HE and clinical image, respectively.

TABLE I. Information on the CT data of the lung cancer patients, that was used to simulate chest radiographs. Patient size is listed as a surrogate for radiological depth.

			Tumor motion (mm)			Patient size (cm)		
Patient No.	Tumor position	GTV (cm^3)	AP	LR	SI	AP	LR	CT resolution (mm^3)
1	Upper right lobe	22	7	2	10	24	39	0.98×0.98×2.0
2	Lower right lobe	4	11	2	11	25	31	1.05×1.05×2.0
3	Lower right lobe	26	2	3	13	23	30	0.96×0.96×2.0
4	Upper left lobe	12	4	1	9	31	48	1.37×1.37×2.0
5	Lower right lobe	12	2	1	7	24	29	0.98×0.98×2.0
6	Upper left lobe	9	3	1	5	24	37	1.04×1.04×2.0

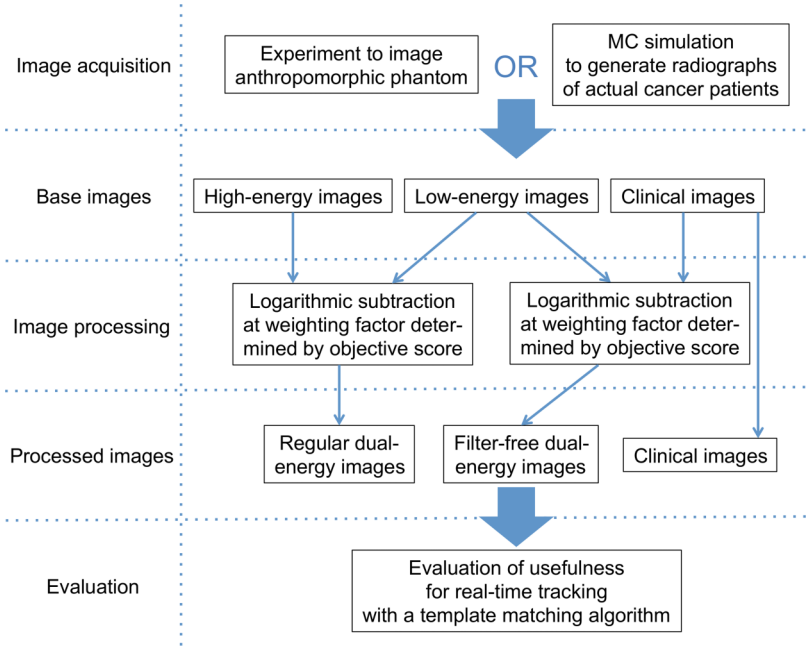

FIG. 2. Schematic describing the study workflow.

2.C. Calculation of dual-energy images

The experimentally acquired and the MC-simulated LE, HE, and clinical radiographs were used to calculate two different types of DE images (see Fig. 2). *Regular dual-energy* (rDE) images were calculated according to

$$\ln(I_{\mathrm{DE}}(x,y)) = \ln(I_{\mathrm{HE}}(x,y)) - w\ln(I_{\mathrm{LE}}(x,y)), \tag{1}$$

where each pixel of the rDE image $I_{\mathrm{DE}}(x,y)$ is calculated by logarithmically subtracting the corresponding pixel value of the HE and LE image $I_{\mathrm{HE}}(x,y)$ and $I_{\mathrm{LE}}(x,y)$ with a patient specific weighting factor w. The weighting factor was optimized between 0.0 and 1.0, so that maximum tumor visibility, measured with an objective score (see Sec. 2.D), was achieved. *Filter-free dual-energy* (ffDE) images were calculated by weighted logarithmic subtraction of the clinical and LE images in order to investigate the influence of the spectral separation of the imaging spectra on the detail of the calculated DE images (see Fig. 3). The created rDE, ffDE, and clinical images were then evaluated with regard to tumor visibility with a novel objective score and their utility for real-time tracking with an automated TMA.

2.D. Measurement of lung tumor visibility with an objective score

Soft-tissue contrast as well as the presence of bones near the tumor site both influence visibility of lung tumors. We developed an objective score that attempts to evaluate both factors and combines them into one metric that allows quantification of the tumor visibility. The contrast $C_{a,b}$ between two tissue types a and b, with intensities of I_a and I_b, is defined as

$$C_{a,b} = \left| \frac{I_a - I_b}{\frac{1}{2}(I_a + I_b)} \right|. \tag{2}$$

The contrast improvement $\mathrm{CI}_{a,b}$ in the DE image compared to the clinical radiograph is thus

$$\mathrm{CI}_{a,b} = \frac{C_{a,b}(\text{DE image})}{C_{a,b}(\text{clinical image})}. \tag{3}$$

The final objective score S comprises the contrast improvement of the tumor-to-lung-tissue contrast, as well as the contrast improvement of the bone-to-lung-tissue and the bone-to-tumor contrast,

$$S = \frac{\mathrm{CI}_{\text{tumor,lung tissue}}}{\frac{1}{2}\left(\mathrm{CI}_{\text{bone,lung tissue}} + \mathrm{CI}_{\text{bone,tumor}}\right)}. \tag{4}$$

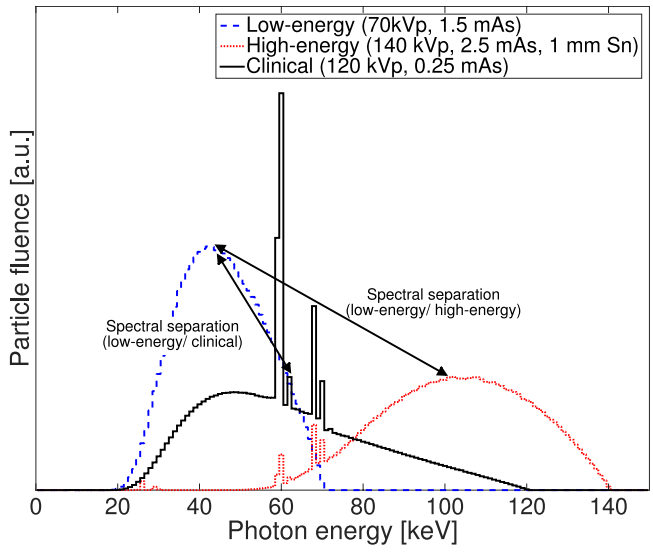

FIG. 3. The MC-simulated spectral distributions of the three imaging beams. The LE and HE beams feature increased spectral separation compared to the LE and clinical beams. This is beneficial to the selectivity of the created DE images.

Higher tumor-to-lung-tissue contrast improvement is desirable and consequently boosts the objective score, while increased bone contrast improvement is detrimental to tumor visibility and decreases the score. The score ranges from 0 to infinity and a score of 1.0 means that the tumor visibility is as high as in the clinical radiograph.

In order to calculate the objective score, the mean intensity of four different image regions is needed: unobscured lung tissue and tumor tissue as well as those two tissue types superimposed with bone. 5×5 pixels large regions of interest were delineated three times by one observer and subsequently the objective score was calculated 81 times for all possible combinations of the input regions of interest. This was done in order to obtain an average score, which was more robust against user bias, tissue inhomogeneities, and image noise during delineation, and also to gain an estimate for the error of the score by calculating the standard deviation of all scores. This objective score allows comparison of different imaging settings as well as different weighting factors used during DE image generation.

2.E. Evaluation of dual-energy images for real-time tracking with a template matching algorithm

An automated TMA, based on work by Wisotzky *et al.*,[34] was developed. This algorithm attempts to localize the tumor using normalized cross correlation (NCC). A rectangular template containing the tumor region plus an additional margin of 3 pixels is user-delineated on the peak-exhale radiographs for each imaging setting being evaluated. The position and size of the templates were kept similar in each specific patient-imaging-angle-combination in order to ensure comparability. The TMA then places this template on all possible positions in a selected subsequent image in a search region of ±2 cm in both directions. For each position, all pixels not covered by the template are cropped from the image and the score NCC is calculated via

$$\mathrm{NCC}=\frac{1}{N}\sum_{x,y}\frac{\left(f(x,y)-\bar{f}\right)\left(t(x,y)-\bar{t}\right)}{\sigma_f\sigma_t}, \tag{5}$$

where $f(x,y)$ and $t(x,y)$ are the pixel values at position (x,y) of the image and template, respectively. $\bar{f}$ and $\bar{t}$ denote the mean pixel values of the image and template. The standard deviations of the pixel values contained in the image and template are σ_f and σ_t, respectively, and N is the total amount of evaluated pixels. This NCC score ranges from −1.0 to 1.0. A higher score indicates a better concordance of the template with the image at the matched position. A negative score indicates inverse correlation between the pixel values in the image and template. In order to speed up this calculation, the OPENCV package was used to calculate the NCC score in Fourier space.[35,36] With this, the TMA takes about 25 ms to match a 125×125 pixels template onto a 512×512 pixels image on a desktop PC with an i7-2600 (Intel Corporation, Santa Clara, CA, USA) processor and 8 GB of RAM.

After calculating the NCC score for all possible template positions, the position with the maximum NCC score is deemed the tumor position. The calculated positions were compared to the true tumor centroid positions, which were manually determined by one observer, in order to obtain the localization error.

3. RESULTS

3.A. Evaluation of dual-energy images of an anthropomorphic breathing chest phantom

The AP and LR radiographs of the Lucy phantom are shown in Fig. 4. The ribs were clearly visible in the images acquired at clinical settings. In the LR radiographs, the heart and spherical tumor appeared superimposed. The AP rDE image with the maximum increase in lung tumor visibility was obtained at a weighting factor of 0.39, at which the objective score reached its maximum of 1.84 [see Fig. 5(a)]. However, the tumor-to-lung-tissue contrast was also reduced. When calculating the ffDE image, the objective score reached its maximum of 1.45 at a weighting factor of 0.71 [see Fig. 5(b)]. Similar weighting factors were determined when using the LR images of the Lucy phantom. When comparing the rDE images to the clinical radiographs, the decreased visibility of the ribs in the tumor region as well as in the lung tissue was clearly recognizable. The ffDE images also featured lower bone visibility compared to the clinical radiographs, but the tumor-to-lung-tissue contrast in the ffDE image decreased even further compared to the contrast in the rDE images. DE imaging was not able to increase the contrast between the superimposed heart and tumor as both structures consist of materials of similar radiodensity.

In AP imaging direction, the TMA was able to localize the tumor very well in the clinical and rDE imaging series [see Fig. 6(a)]. With the ffDE imaging series, a lower tracking accuracy was achieved. In LR direction, it was not possible to register the clinical and LE imaging series due to phantom hysteresis induced by the warming up of the lung compartment. Consequently, only the rDE series was compared to the clinical imaging series. Here, the templates included parts of the heart superimposed with the tumor. The TMA struggled to localize the tumor regardless of which dynamic imaging series was used as input [see Fig. 6(b)]. The measurement was repeated using smaller templates including only the part of the tumor not superimposed by heart tissue. With the small templates, the TMA was able to determine the tumor position with a very high accuracy when using the rDE imaging series as input, while it was inaccurate when using clinical input radiographs [see Fig. 6(c)].

3.B. Evaluation of simulated dual-energy images of lung cancer patients

rDE and ffDE images of actual lung cancer patients were calculated using the MC-simulated LE, HE, and clinical radiographs (see Figs. 7–10). When calculating rDE images, the maximum objective score ranged from 2.03 to 3.53 at a weighting factor varying between 0.15 and 0.26. During

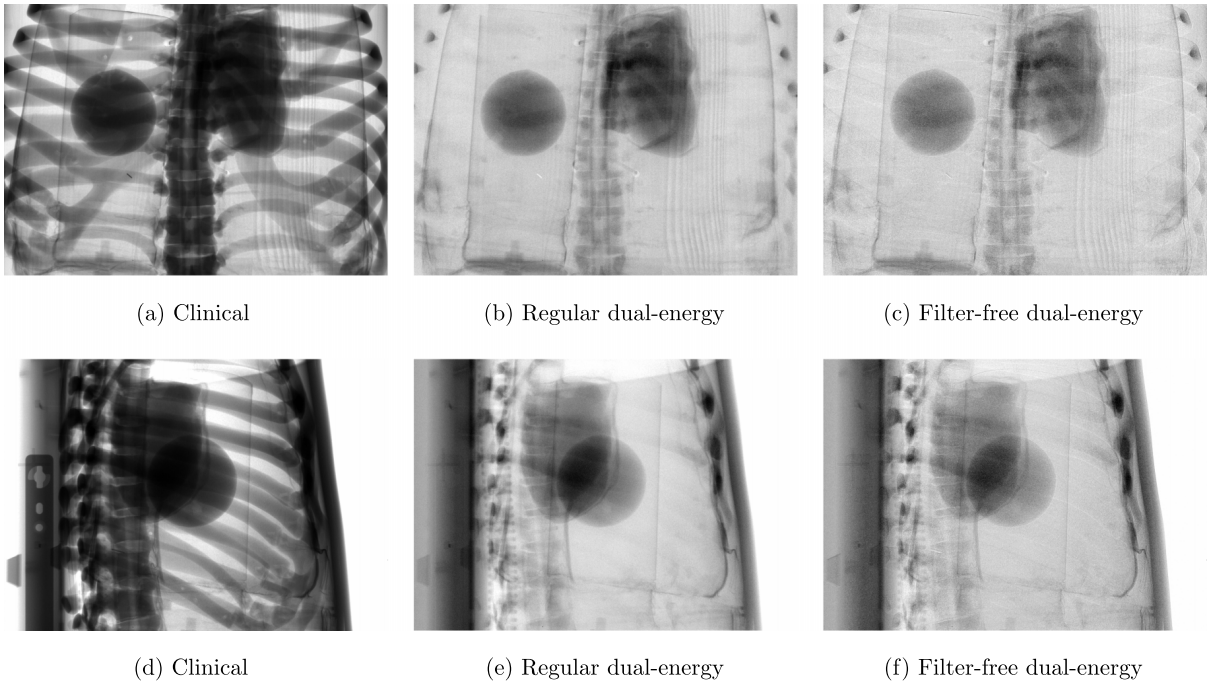

(a) Clinical (b) Regular dual-energy (c) Filter-free dual-energy

(d) Clinical (e) Regular dual-energy (f) Filter-free dual-energy

FIG. 4. Experimentally acquired radiographs of the Lucy phantom in [(a)–(c)] AP imaging direction and [(d)–(f)] LR imaging direction. The windowing settings in all images were set based on the minimum and maximum intensity in the lung.

evaluation of the ffDE images, the objective score reached a maximum ranging between 1.53 and 2.23. The weighting factor varied between 0.42 and 0.53. An example is shown in Fig. 11 for the AP images of patient 1, where the objective score reached 2.23 at a weighting factor of 0.16 for the rDE image and 1.74 at a weighting factor of 0.46 for the ffDE image. A tendency for lower maximum objective scores at lower ideal weighting factors was observed when the imaging beam had to traverse more tissue due to patient size or imaging angle. At some patient-imaging-angle-combinations, it was not possible to generate a template for the TMA or to robustly delineate regions of interest to calculate the objective score. These cases were deemed as "failed".

The localization accuracy of the TMA depending on the input radiograph type is shown in Fig. 12 for all patients and beam angles. When using rDE images in place of clinical radiographs, tracking accuracy increased in 7 out of 24 cases, remained comparable (less than 0.5 mm change in tracking accuracy) in 3 out of 24 cases, and worsened in 5 out of 24 cases. ffDE imaging performed better in only 2 out of 24 cases, comparable in 4 out of 24 cases, and worse in 9 out of 24 cases. In 9 out of 24 cases, it was not possible to define a template for the TMA regardless of the type of radiograph used due to

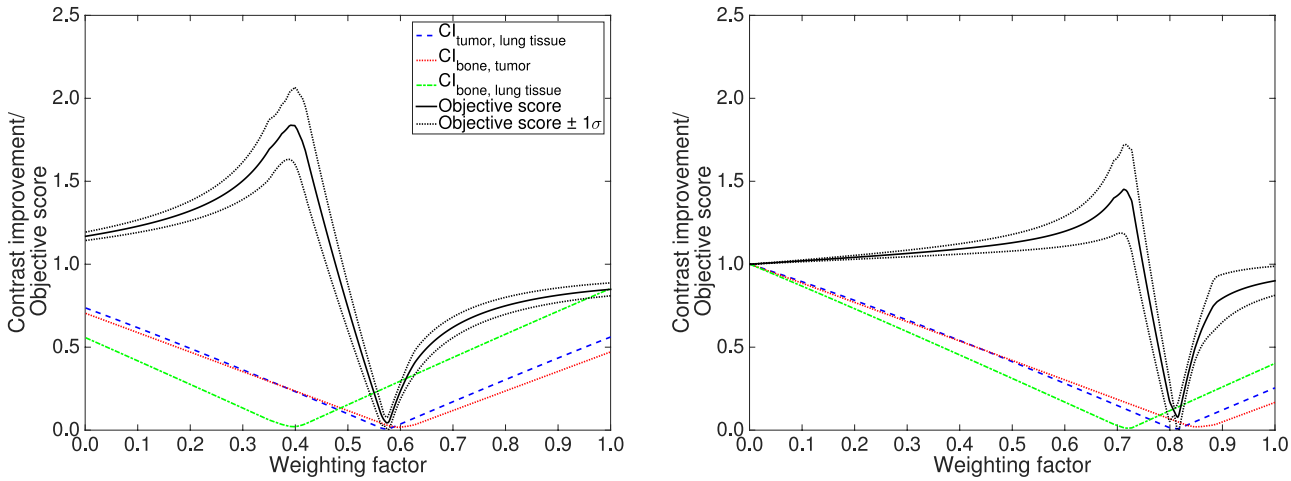

(a) Regular dual-energy (b) Filter-free dual-energy

FIG. 5. Contrast improvement and objective score depending on the weighting factor in the rDE and ffDE images of the Lucy phantom.

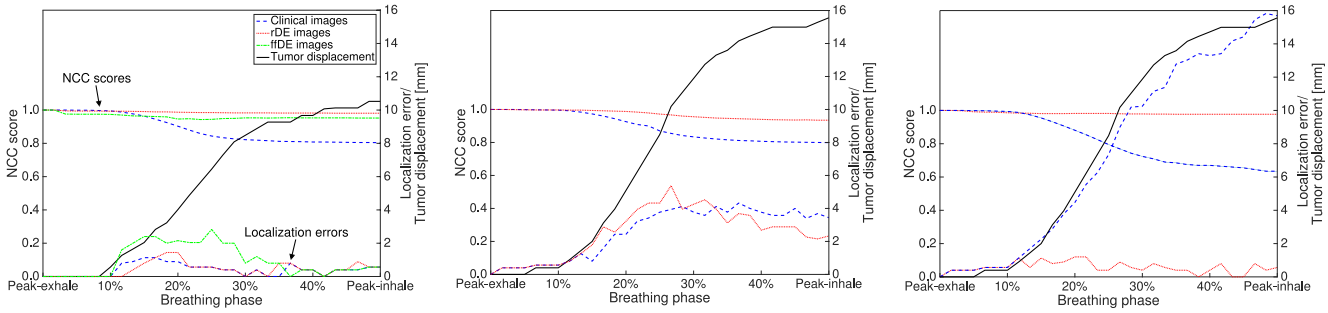

(a) AP imaging series (b) LR imaging series - large template (c) LR imaging series - small template

FIG. 6. The NCC score and localization error of the TMA for different input imaging series of the Lucy phantom.

insufficient soft-tissue contrast. The mean localization errors using clinical, rDE, and ffDE radiographs were 3.85, 3.32, and 5.24 mm, respectively.

A case in which both rDE and ffDE imaging improved tracking accuracy in patient 3 is shown in Fig. 7. At the 135° imaging angle, vision of the tumor was impaired by ribs as well as the spine. Dual-energy imaging was able to reduce the visibility of these bony structures. The geometry of patient 5 was comparable. However, in that patient the reduction of the visibility of the spine through DE imaging did not lead to a further increase in tracking accuracy, which was already very high using clinical images. If the tumor was superimposed with other large soft-tissue structures, like the hilum, mediastinum or heart, as in patient 1 at an imaging angle of 45°, dual-energy imaging was usually not able to increase tracking accuracy, even though it reduced the visibility of bones (see Fig. 8). In patient 4, the largest of the six patients, low signal-to-noise-ratio inhibited the tracking accuracy. For this patient, it was impossible to localize the tumor and define a template in any imaging direction except AP. Dual-energy imaging could not resolve this problem. Definition of the template was also hindered in the AP and 45° images of patient 2. The small tumor was located on the posterior side of the diaphragm, which obscured the view of the tumor at these imaging angles (see Fig. 9). An example of a failed patient-imaging-angle-combination is shown in Fig. 10 for the radiographs acquired at 45° for patient 6.

4. DISCUSSION

4.A. Findings of this study

For both phantom and simulated patient radiographs, DE imaging was able to increase tracking accuracy in several cases in which the tumor was primarily covered by bony anatomy. However, it has also been shown that DE imaging is governed by some of the same shortcomings as single-energy projection x-ray imaging. Superposition of the tumor with other soft-tissue anatomy, such as the mediastinum, diaphragm, or heart cannot be resolved in the DE radiographs. Additionally, imaging through a large amount of tissue increases scatter and thereby decreases image contrast. Due to these effects the success of automated tumor localization is very dependent on tumor position, tumor size, imaging beam angle, and patient size.

Recently, Sherertz *et al.*[18] have investigated DE imaging for image-guided radiotherapy. They acquired DE images of ten different patients with 11 lung tumors. They found that DE imaging was able to increase both contrast and contrast-to-noise ratio compared to single-energy imaging. Higher contrast improvement was achieved for larger tumors and they reported that the two smallest tumors could not be reliably visualized. This study found a similar dependency of tracking success on the tumor size as smaller tumors were less visible, especially when being obscured by other soft-tissue structures. Additionally, Sherertz *et al.*[18] reported that a physician was

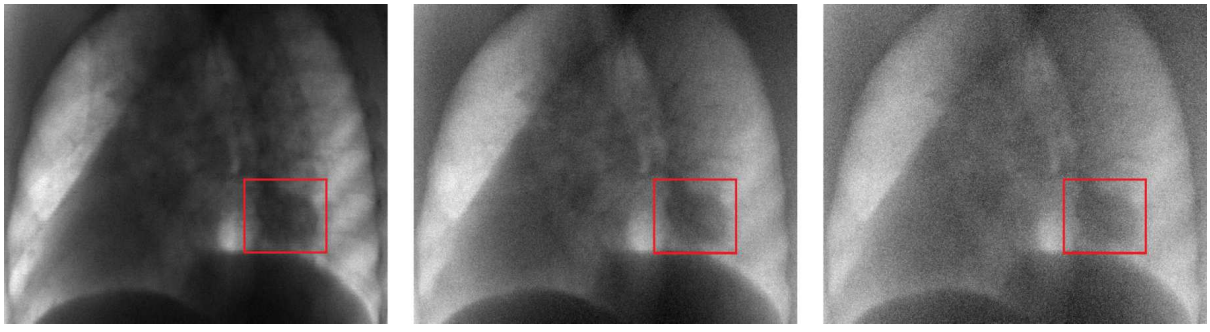

(a) Clinical (b) Regular dual-energy (c) Filter-free dual-energy

FIG. 7. Simulated radiographs of patient 3 at an imaging angle of 135°. The red box indicates the tumor position. In this case DE imaging was able to reduce the prominence of bones and increased the tracking accuracy.

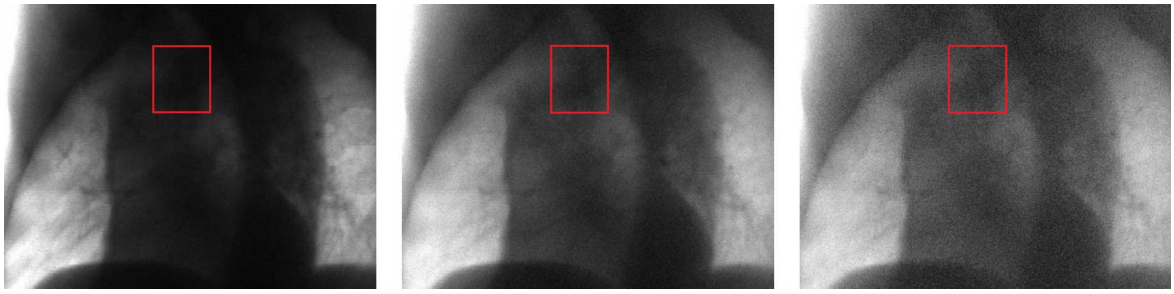

(a) Clinical (b) Regular dual-energy (c) Filter-free dual-energy

FIG. 8. Simulated radiographs of patient 1 at an imaging angle of 45°. Tumor localization was only possible with a high error regardless of imaging settings due to the superposition of the tumor and mediastinum.

able to localize the tumor in 95% of DE images and only 74% of single-energy images. However, in a real-time adaptive radiotherapy workflow, manual tumor localization is not an option.

Similar to this study, Patel *et al.*[19] used a TMA based on NCC to localize the tumor in DE images of a phantom and two lung cancer patients. They define their template based on a previously acquired CT scan, while this study outlines the template in the corresponding projection kV images. Their reported 95th percentile absolute tracking errors for the two patients were 2.5 and 6.0 mm for single-energy radiographs and 2.5 and 3.9 mm for dual-energy radiographs. The tracking accuracies determined in this study are comparable to this, as the investigated matching of a peak-exhale template onto the peak-inhale phase usually constitutes the most challenging task due to reduced mutual information between the two phases. However, in their study the TMA was able to localize the tumor in all patient images, both single-energy images as well as DE radiographs, while this study has also presented cases, where template definition was not possible. They concluded that DE imaging can potentially enhance real-time markerless tumor tracking while pointing out the importance of patient anatomy, which our study has followed up on by specifically having investigated patient cases, in which automated localization of the target is difficult. Future work should aim at quantitatively describing the correlation between anatomical characteristics and the feasibility of DE imaging to improve tracking accuracy.

Furthermore, this study has investigated the effect of spectral separation of the imaging beams on the success rate of tumor tracking. It has been shown that higher spectral separation of the two imaging beams increases the selectivity of the calculated DE radiographs. However, the maximum achievable separation is limited due to the polychromatic nature of the imaging beams and the fact that additional filters increase photon scatter and require modifications of the x-ray tube. In the future, photon counting detectors might allow acquisition of images with high spectral separation and, consequently, more detailed DE images.[37] However, their application is currently limited due to their low tolerable photon fluence rates, small detector sizes, and high production costs.

4.B. Shortcomings of and possible improvements to the used methodology

The Lucy phantom is one of the only anthropomorphic chest phantoms featuring differential motion of the ribs and lung tumor, which is one of the main obstacles to overcome during automated lung tumor localization. Still, as with any phantom, the acquired images of it were not completely realistic. The low radiodensity of the foam material used as lung tissue, the nonhollow ribs, and the simplistic phantom

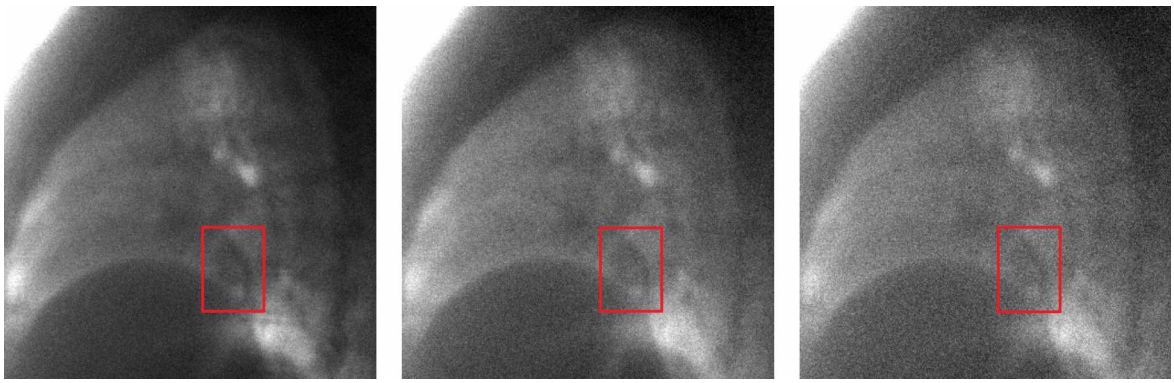

(a) Clinical (b) Regular dual-energy (c) Filter-free dual-energy

FIG. 9. Simulated radiographs of patient 2 in LR imaging direction. The small tumor, which was located posterior of the diaphragm, made localization impossible at the AP and 45° imaging angle.

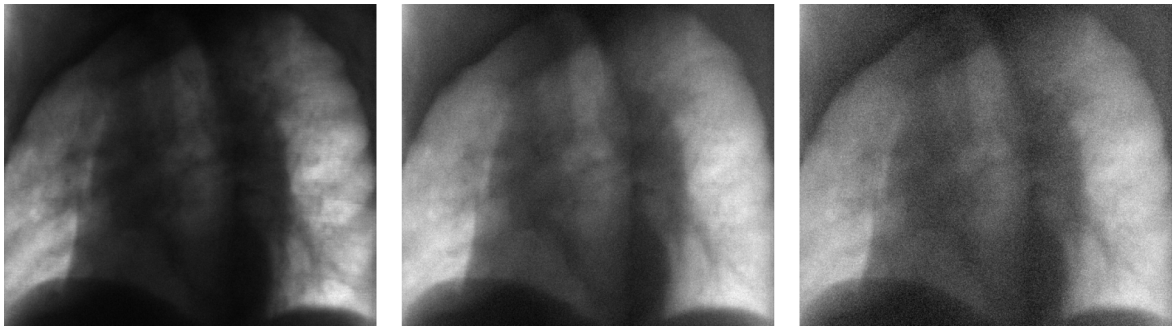

(a) Clinical (b) Regular dual-energy (c) Filter-free dual-energy

FIG. 10. Simulated radiographs of patient 6 at an imaging angle of 45°. In this failed case, it was not possible to clearly identify the tumor and generate a template for the TMA.

geometry led to a higher tumor-to-lung-tissue contrast and lower image noise than one would expect in human chest radiographs. Phantom deformation in between experiments or over the course of long measurements caused image artifacts due to registration errors.

The experimental setup would not have been able to reliably acquire DE images of an actual patient. In the experiments, the entire LE, HE, and clinical imaging series were obtained sequentially instead of repeatedly acquiring LE–HE or LE–clinical image pairs in quick succession. The latter approach is necessary in order to obtain DE images in real-time without registration artifacts due to changes in patient anatomy and gantry angle. A DE imaging system for a real-time adaptive radiotherapy application would require a fast kVp-switching x-ray tube and a FPD allowing quick acquisition of kV images. If additional beam filtration is desired at one imaging setting, a filter wheel could be used to change filters in between acquisition modes.[38] However, most current radiotherapy systems do not feature such a filter wheel in their x-ray tubes. All aforementioned components already exist and medPhoton (Salzburg, Austria) has developed a prototype add-on system, allowing real-time acquisition of DE images of patients undergoing radiotherapy. However, to our knowledge, DE imaging utilizing the components featured on an already available clinical linear accelerator has not been realized yet.

Continuous x-ray imaging during radiotherapy results in an additional dose to the patient. Because two images are required for dual-energy imaging, an even higher imaging dose might be induced, although Shkumat *et al.*[39] have demonstrated that it is possible to acquire DE images with enhanced soft-tissue contrast without increasing patient dose. Either way, the imaging dose delivered to healthy tissue is much lower than the dose induced by the treatment beam. Decreasing the treatment safety margins around the tumor to ensure target coverage or preventing missing the tumor might outweigh the additional dose. Discussion of the exact trade-off between added anatomical information about the patient during treatment and higher imaging dose is beyond the scope of this work.

It was shown that the developed MC simulation produces results agreeing well with experimental measurements and results published in the literature[30–32] (see Appendix A of the supplementary material[33]). With it we were able to investigate the feasibility of markerless tumor tracking in DE radiographs of lung cancer patients without some of the aforementioned problems of experimental image acquisitions such as patient dose constraints and registration errors. In a clinical scenario,

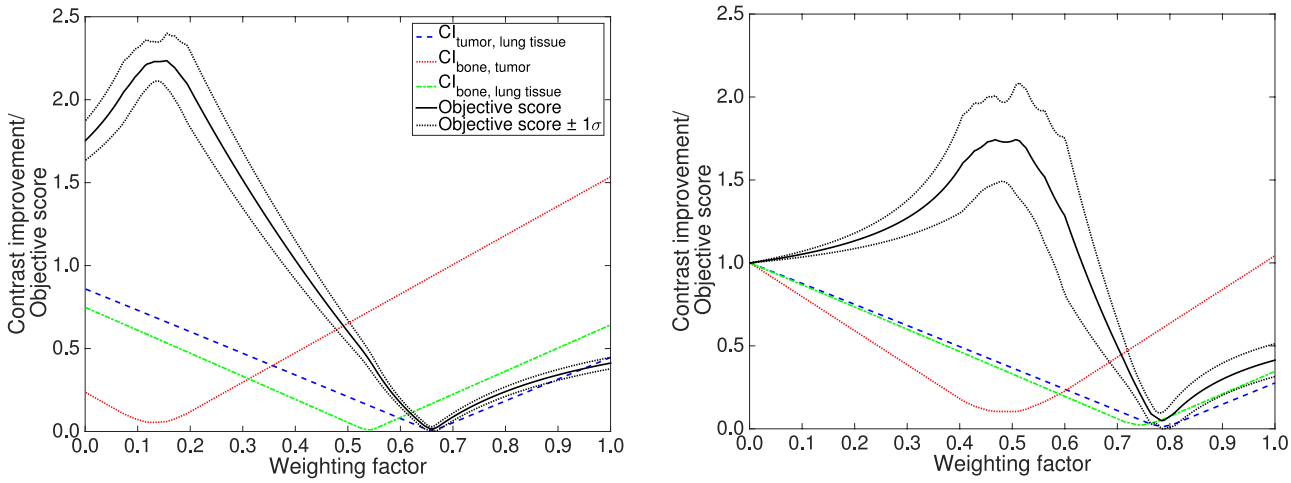

(a) Regular dual-energy (b) Filter-free dual-energy

FIG. 11. Contrast improvement and objective score depending on the weighting factor in the rDE and ffDE images of patient 1 acquired in AP direction.

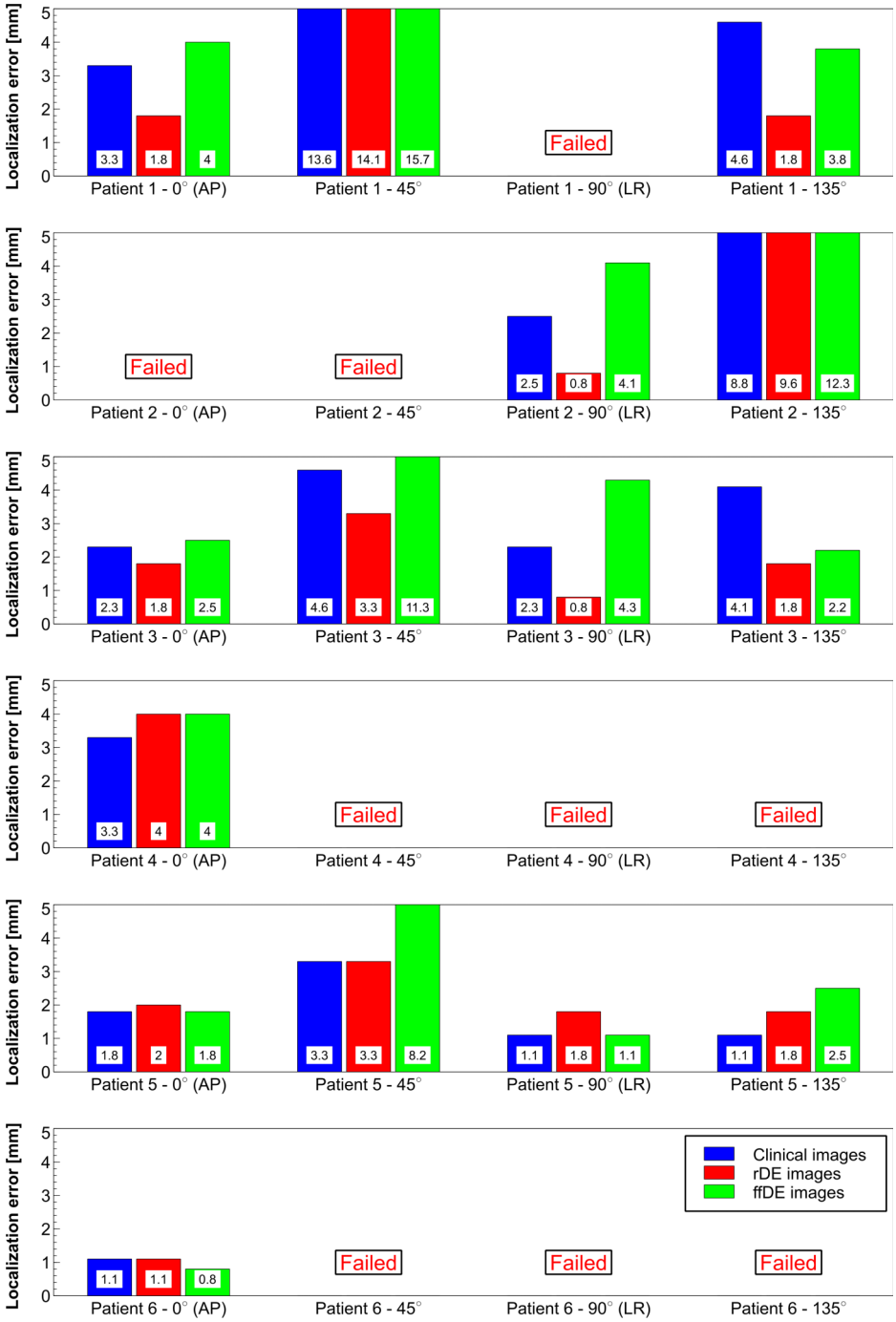

FIG. 12. Localization error of the TMA for all investigated patient-imaging-angle-combinations. In the failed cases, it was not possible to create a tumor template due to poor tumor visibility. The y-axis is cropped at 5 mm.

MC simulations could be used to generate the tumor template, determine the ideal weighting factor for logarithmic subtraction, and identify potentially difficult patient geometries and imaging angles from the planning CT prior to treatment. However, some limitations and inaccuracies remain. Due to the limit in computational time, the simulated radiographs featured higher noise than experimentally acquired images. Instead of a full-scale MC framework, digitally reconstructed radiographs with convoluted scatter and noise kernels might be deployed for template generation as a less computationally intensive alternative.[40] Other problems lay with the 4DCT data used as input for the MC simulation. Besides some motion artifacts arising from changes in patient geometry during 4DCT acquisition,[41] the ribs were less pronounced in the generated radiographs due to the partial volume effect (see Appendix B of the supplementary material[33] for more details).

The TMA used in this work is a very basic implementation of NCC. More advanced methods include evaluation of the slope of the NCC score around the derived target position.[42] Others have investigated updating the template over the course of the tracking.[43] Although this requires high confidence in the determined tumor position and safeguarding against

so-called "template drifting," it allows compensation for gradual changes in the shape of the tumor or surrounding landmarks. The accuracy of template matching depends on the size of the template and, consequently, the amount of surrounding landmarks included in the template. Potentially, the use of irregularly shaped templates excluding such landmarks could result in a higher localization accuracy, although this is not possible if the tumor and landmark overlap.

5. CONCLUSIONS

This study has highlighted the influence of patient anatomy on the success rate of real-time markerless tumor tracking using DE imaging. Additionally, the importance of the spectral separation of the imaging beams used to generate the DE images has been shown. While DE imaging can increase tracking accuracy in some cases, clinical deployment of real-time DE tumor tracking in its current state would rely on preselection of suitable lung cancer patients.

ACKNOWLEDGMENTS

The authors would like to thank Paul-Scherrer-Institut and Centre Suisse d'Electronique et Microtechnique for lending them the anthropomorphic phantom and Dr. Antje Knopf for her help setting up this collaboration and with the transport of the phantom. The authors thank Jamie A. Dean for improving the clarity of this manuscript and Vibeke N. Hansen and Helen McNair for their help obtaining the patient CT scans. The authors acknowledge support from Elekta AB under a research agreement. Research at The Institute of Cancer Research is also supported by Cancer Research UK under Programme No. C33589/A19727. The authors acknowledge NHS funding to the NIHR Biomedical Research Centre at The Royal Marsden and The Institute of Cancer Research.

[a]Electronic mail: martin.menten@icr.ac.uk
[b]Electronic mail: uwe.oelfke@icr.ac.uk

[1]P. J. Keall, G. S. Mageras, J. M. Balter, R. S. Emery, K. M. Forster, S. B. Jiang, J. M. Kapatoes, D. A. Low, M. J. Murphy, B. R. Murray, C. R. Ramsey, M. B. Van Herk, S. S. Vedam, J. W. Wong, and E. Yorke, "The management of respiratory motion in radiation oncology report of AAPM Task Group 76," Med. Phys. **33**, 3874–3900 (2006).
[2]M. Hoogeman, J. B. Prevost, J. Nuyttens, J. Poll, P. Levendag, and B. Heijmen, "Clinical accuracy of the respiratory tumor tracking system of the cyberknife: Assessment by analysis of log files," Int. J. Radiat. Oncol., Biol., Phys. **74**, 297–303 (2009).
[3]Y. Matsuo, N. Ueki, K. Takayama, M. Nakamura, Y. Miyabe, Y. Ishihara, N. Mukumoto, S. Yano, H. Tanabe, S. Kaneko, T. Mizowaki, H. Monzen, A. Sawada, M. Kokubo, and M. Hiraoka, "Evaluation of dynamic tumour tracking radiotherapy with real-time monitoring for lung tumours using a gimbal mounted linac," Radiother. Oncol. **112**, 360–364 (2014).
[4]W. D. D'Souza, S. A. Naqvi, and C. X. Yu, "Real-time intra-fraction-motion tracking using the treatment couch: A feasibility study," Phys. Med. Biol. **50**, 4021–4033 (2005).
[5]J. Wilbert, J. Meyer, K. Baier, M. Guckenberger, C. Herrmann, R. Heß, C. Janka, L. Ma, T. Mersebach, A. Richter, M. Roth, K. Schilling, and M. Flentje, "Tumor tracking and motion compensation with an adaptive tumor tracking system (ATTS): System description and prototype testing," Med. Phys. **35**, 3911–3920 (2008).
[6]P. J. Keall, V. R. Kini, S. S. Vedam, and R. Mohan, "Motion adaptive x-ray therapy: A feasibility study," Phys. Med. Biol. **46**, 1–10 (2001).
[7]M. Tacke, S. Nill, and U. Oelfke, "Real-time tracking of tumor motions and deformations along the leaf travel direction with the aid of a synchronized dynamic MLC leaf sequencer," Phys. Med. Biol. **52**, N505–N512 (2007).
[8]M. F. Fast, S. Nill, J. L. Bedford, and U. Oelfke, "Dynamic tumor tracking using the Elekta Agility MLC," Med. Phys. **41**, 111719 (5pp.) (2014).
[9]B. Cho, P. R. Poulsen, A. Sloutsky, A. Sawant, and P. J. Keall, "First demonstration of combined kV/MV image-guided real-time dynamic multileaf-collimator target tracking," Int. J. Radiat. Oncol., Biol., Phys. **74**, 859–867 (2009).
[10]M. F. Fast, A. Krauss, U. Oelfke, and S. Nill, "Position detection accuracy of a novel linac-mounted intrafractional x-ray imaging system," Med. Phys. **39**, 109–118 (2012).
[11]A. Sawant, R. L. Smith, R. B. Venkat, L. Santanam, B. Cho, P. Poulsen, H. Cattell, L. J. Newell, P. Parikh, and P. J. Keall, "Toward submillimeter accuracy in the management of intrafraction motion: The integration of real-time internal position monitoring and multileaf collimator target tracking," Int. J. Radiat. Oncol., Biol., Phys. **74**, 575–582 (2009).
[12]A. Krauss, S. Nill, M. Tacke, and U. Oelfke, "Electromagnetic real-time tumor position monitoring and dynamic multileaf collimator tracking using a Siemens 160 MLC: Geometric and dosimetric accuracy of an integrated system," Int. J. Radiat. Oncol., Biol., Phys. **79**, 579–587 (2011).
[13]W. R. Brody, "A method for selective tissue and bone visualization using dual energy scanned projection radiography," Med. Phys. **8**, 353–357 (1981).
[14]J.-T. Ho, "Comparison of dual and single exposure techniques in dual-energy chest radiography," Med. Phys. **16**, 202–208 (1989).
[15]J. M. Sabol, G. B. Avinash, F. Nicolas, B. E. H. Claus, J. Zhao, and J. T. Dobbins III, "Development and characterization of a dual-energy subtraction imaging system for chest radiography based on CsI:Tl amorphous silicon flat-panel technology," Proc. SPIE **4320**, 399–408 (2001).
[16]T. Xu, J. L. Ducote, J. T. Wong, and S. Molloi, "Dynamic dual-energy chest radiography: A potential tool for lung tissue motion monitoring and kinetic study," Phys. Med. Biol. **56**, 1191–1205 (2011).
[17]M. A. Hoggarth, J. Luce, F. Syeda, T. S. Bray, A. Block, S. Nagda, and J. C. Roeske, "Dual energy imaging using a clinical on-board imaging system," Phys. Med. Biol. **58**, 4331–4340 (2013).
[18]T. Sherertz, M. Hoggarth, J. Luce, A. M. Block, S. Nagda, M. M. Harkenrider, B. Emami, and J. C. Roeske, "Prospective evaluation of dual-energy imaging in patients undergoing image guided radiation therapy for lung cancer: Initial clinical results," Int. J. Radiat. Oncol., Biol., Phys. **89**, 525–531 (2014).
[19]R. Patel, J. Panfil, M. Campana, A. M. Block, M. M. Harkenrider, M. Surucu, and J. C. Roeske, "Markerless motion tracking of lung tumors using dual-energy fluoroscopy," Med. Phys. **42**, 254–262 (2015).
[20]M. A. Flower, *Webb's Physics of Medical Imaging* (CRC Press, Boca Raton, FL, 2012).
[21]A. N. Primak, J. C. Ramirez Giraldo, X. Liu, L. Yu, and C. H. McCollough, "Improved dual-energy material discrimination for dual-source CT by means of additional spectral filtration," Med. Phys. **36**, 1359–1369 (2009).
[22]S. Agostinelli *et al.*, "GEANT4—A simulation toolkit," Nucl. Instrum. Methods Phys. Res., Sect. A: Accel., Spectrom., Detect. Assoc. Equip. **506**, 250–303 (2003).
[23]J. Baró, J. Sempau, J. M. Fernández-Varea, and F. Salvat, "PENELOPE: An algorithm for Monte Carlo simulation of the penetration and energy loss of electrons and positrons in matter," Nucl. Instrum. Methods Phys. Res., Sect. B: Beam Interact. Mater. At. **100**, 31–46 (1995).
[24]XVI R5.0 instructions for use for Elekta Synergy, Elekta Axesse, Elekta Infinity, Versa HD (2013).
[25]W. Schneider, T. Bortfeld, and W. Schlegel, "Correlation between CT numbers and tissue parameters needed for Monte Carlo simulations of clinical dose distributions," Phys. Med. Biol. **45**, 459–478 (2000).
[26]D. W. Smith, D. Christophides, C. Dean, M. Naisbit, J. Mason, and A. Morgan, "Dosimetric characterization of the iBEAM evo carbon fiber couch for radiotherapy," Med. Phys. **37**, 3595–3606 (2010).
[27]A. E. Schach von Wittenau, C. M. Logan, M. B. Aufderheide, and D. M. Slone, "Blurring artifacts in megavoltage radiography with a flat-panel imaging system: Comparison of Monte Carlo simulations with measurements," Med. Phys. **29**, 2559–2570 (2002).
[28]L. Parent, J. Seco, P. M. Evans, A. Fielding, and D. R. Dance, "Monte Carlo modelling of a-Si EPID response: The effect of spectral variations with field size and position," Med. Phys. **33**, 4527–4540 (2006).

[29]M. F. Fast, A. Teymurazyan, G. Pang, U. Oelfke, and J. A. Rowlands, "Finding an improved amorphous-silicon x-ray flat-panel detector configuration for the in-line geometry," Phys. Med. Biol. **58**, 2305–2324 (2013).
[30]E. Spezi, P. Downes, E. Radu, and R. Jarvis, "Monte Carlo simulation of an x-ray volume imaging cone beam CT unit," Med. Phys. **36**, 127–136 (2009).
[31]P. Downes, R. Jarvis, E. Radu, I. Kawrakow, and E. Spezi, "Monte Carlo simulation and patient dosimetry for a kilovoltage cone-beam CT unit," Med. Phys. **36**, 4156–4167 (2009).
[32]G. Jarry, S. A. Graham, D. J. Moseley, D. J. Jaffray, J. H. Siewerdsen, and F. Verhaegen, "Characterization of scattered radiation in kV CBCT images using Monte Carlo simulations," Med. Phys. **33**, 4320–4329 (2006).
[33]See supplementary material at http://dx.doi.org/10.1118/1.4935431 for a description of the simulations and experiments conducted to validate the developed Monte Carlo simulation and a description of the effects of the partial volume effect on the simulated radiographs.
[34]E. Wisotzky, M. F. Fast, U. Oelfke, and S. Nill, "Automated marker tracking using noisy x-ray images degraded by the treatment beam," Z. Med. Phys. **25**, 123–134 (2015).
[35]J. P. Lewis, "Fast template matching," Vision Interface **10**, 120–123 (1995).
[36]G. Bradski, "The OPENCV library," Doctor Dobbs Journal of Software Tools (2000).
[37]K. Rink, T. Koenig, M. Zuber, A. Zwerger, A. Fauler, M. Fiederle, and U. Oelfke, "Saturation effects of CdTe photon counting detectors under high photon fluxes," J. Instrum. **8**, C01026 (2013).
[38]M. Spahn, "System and method for real time dual energy x-ray image acquisition," U.S. patent No. 7,463,715 (9 December 2008).
[39]N. A. Shkumat, J. H. Siewerdsen, A. C. Dhanantwari, D. B. Williams, S. Richard, N. S. Paul, J. Yorkston, and R. Van Metter, "Optimization of image acquisition techniques for dual-energy imaging of the chest," Med. Phys. **34**, 3904–3915 (2007).
[40]S. Tang, H. Yu, H. Yan, D. Bharkhada, and X. Mou, "X-ray projection simulation based on physical imaging model," J. X-Ray Sci. Technol. **14**, 177–190 (2006).
[41]T. Yamamoto, U. Langner, B. W. Loo, Jr., J. Shen, and P. J. Keall, "Retrospective analysis of artifacts in four-dimensional CT images of 50 abdominal and thoracic radiotherapy patients," Int. J. Radiat. Oncol., Biol., Phys. **72**, 1250–1258 (2008).
[42]M. Debella-Gilo and A. Kääb, "Sub-pixel precision image matching for measuring surface displacements on mass movements using normalized cross-correlation," Remote Sens. Environ. **115**, 130–142 (2011).
[43]I. Matthews, T. Ishikawa, and S. Baker, "The template update problem," IEEE Trans. Pattern Anal. Mach. Intell. **26**, 810–815 (2004).